

Intangible pointlike tracers for liquid-crystal-based microsensorsEtienne Brasselet^{1,*} and Saulius Juodkazis²¹*Centre de Physique Moléculaire Optique et Hertzienne, Université Bordeaux I, CNRS, 351 Cours de la Libération, 33405 Talence Cedex, France*²*Centre for Micro-Photonics, Faculty of Engineering and Industrial Sciences, Swinburne University of Technology, Hawthorn, Victoria 3122, Australia*

(Received 27 October 2010; published 28 December 2010)

We propose an optical detection technique for liquid-crystal-based sensors that is based on polarization-resolved tracking of optical singularities and does not rely on standard observation of light-intensity changes caused by modifications of the liquid crystal orientational ordering. It uses a natural two-dimensional network of polarization singularities embedded in the transverse cross section of a probe beam that passes through a liquid crystal sample, in our case, a nematic droplet held in laser tweezers. The identification and spatial evolution of such a topological fingerprint is retrieved from subwavelength polarization-resolved imaging, and the mechanical constraint exerted on the molecular ordering by the trapping beam itself is chosen as the control parameter. By restricting our analysis to one type of point singularity, C points, which correspond to location in space where the polarization azimuth is undefined, we show that polarization singularities appear as intangible pointlike tracers for liquid-crystal-based three-dimensional microsensors. The method has a superresolution potential and can be used to visualize changes at the nanoscale.

DOI: [10.1103/PhysRevA.82.063832](https://doi.org/10.1103/PhysRevA.82.063832)

PACS number(s): 42.70.Df, 42.25.Ja, 61.30.Gd

I. INTRODUCTION

Deformable materials have a prominent role in biochemical and physical sensing applications. Nowadays, microfabrication technologies allow for the design of miniaturized two-dimensional (2D) arrays of inorganic or organic sensors on a single chip. Despite having a less mature technology compared with their inorganic counterpart, organic materials offer several key advantages, such as low-cost fabrication and the ability to be processed on flexible substrates. Indeed, one decade ago, the promising potential of organic transistors was revealed [1,2]. This led, for instance, to artificial skin applications [3] and the development of smart devices able to realize point-of-care diagnosis [4].

Besides electrically powered sensors, liquid crystals (LCs) were early recognized as passive chemical or physical detectors that could operate without a power supply. Their principle of operation is merely based on the visual detection between crossed polarizers of the molecular realignment of a LC layer induced by the chemical contamination [5] or the application of physical constraints of a thermal, mechanical, electrical, magnetic, or electromagnetic nature [6]. More recently, the use of the long-range orientational order of LCs has been proved efficient for the optical detection of ligand-receptor binding [7] and, more generally, of biomolecular interactions [8]. In all these cases, *global light intensity or polarization changes* are the key ingredient. In contrast, here, we propose an alternative technique based on the detection of *local changes in the spatial distribution of the polarization of light*.

Optical fields are described as complex vector fields whose amplitude, phase, or polarization may exhibit singularities. Although wave singularities were unveiled in the 1830s, as noticed in [9], they gained a great deal of attention only recently following the publication of seminal papers on phase

singularities [10] and polarization singularities of electromagnetic fields [11]. By combining the orientational sensitivity of LCs with the appearance of a network of well-defined polarization singularities when a light beam propagates inside anisotropic media [12], we suggest that LC-based sensors may benefit from the identification of such intangible fingerprints and their evolution depending on orientational changes. In particular, the self-organization of LCs into droplets allows us to envisage the realization of well-controlled 3D sensors at the micron scale.

Here, we restrict our analysis to the identification and tracking of one type of polarization singularity, the C points [11], which are embedded in the transverse cross section of a probe beam that passes through a nematic LC droplet whose orientational state can be independently tuned by a pump beam. By definition, C points are isolated points where the polarization azimuth of the polarization ellipse is undefined, and they correspond to points of circular polarization embedded in a spatially varying polarization pattern. Their precise observation is carried out experimentally owing to polarization-resolved imaging. In practice, we use a nematic droplet held by laser tweezers, which allows us to accurately control orientational changes in the bulk of the droplet as shown in [13]. Hereafter, we present the experimental setup. Then, we present the identification of three different types of C points and their spatial location dependence on the amplitude of the light-induced orientational perturbation inside the droplet. Finally, we discuss the proposed approach in the framework of related studies before we present our conclusion.

II. OPTICAL TRAPPING AND POLARIZATION-RESOLVED IMAGING

The experimental setup is depicted in Fig. 1. We used the LC material 4'-*n*-pentyl-4-cyanobiphenyl (5CB), which is in the nematic phase at room temperature. When 5CB

*e.brassel@cpmoh.u-bordeaux1.fr

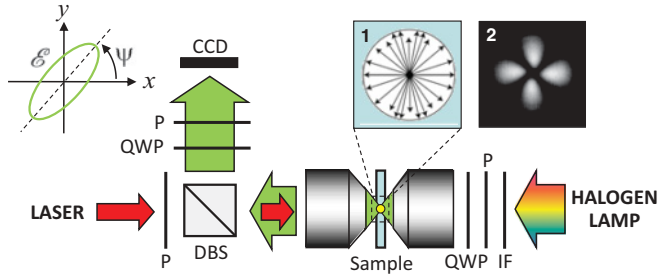


FIG. 1. (Color online) Optical trapping setup at 1064 nm with polarization-resolved imaging at 532 nm. P, polarizer; DBS, dichroic beam splitter; IF, interferential filter at 532 nm; QWP, quarter-wave plate; CCD, charge-coupled device imaging device. The local polarization ellipse \mathcal{E} in the observation plane is illustrated on the left part of the figure, where ψ refers to its azimuth angle. Insets: optical axis distribution of an undistorted radial nematic liquid crystal droplet (panel 1) and its image under crossed polarizers (panel 2).

is dispersed in heavy water (D_2O) spherical droplets are spontaneously formed whose diameter distribution is roughly controlled by shaking the solution. By adding a surfactant (hexadecyltrimethylammonium bromide, CTAB) at a typical concentration of 10^{-5} mol l^{-1} these droplets adopt a spherically symmetric 3D distribution of the local averaged molecular orientation [14]. We refer to such an orientational ordering as a radial alignment; see panel 1 of Fig. 1, which is experimentally identified from the observation of a dark cross when looking at a droplet between crossed polarizers as shown in the panel 2 of Fig. 1. These radial droplets are trapped using a high numerical aperture (NA of 1.3) oil-immersion microscope objective and a linearly polarized continuous-wave laser operating at 1064 nm (heavy water was used to minimize laser-induced temperature rise at this wavelength).

The polarization-resolved imaging of an optically trapped radial droplet is done at 532 nm wavelength by using a spectrally filtered halogen lamp whose polarization state is set as circular by means of a polarizer and a quarter-wave plate placed in front the lamp (see Fig. 1). Then, by placing suitable combinations of polarization optical elements in front of the CCD camera, the four Stokes parameters $S_0 = |E_x|^2 + |E_y|^2$, $S_1 = |E_x|^2 - |E_y|^2$, $S_2 = 2\text{Re}(E_x^*E_y)$, and $S_3 = 2\text{Im}(E_x^*E_y)$ of the output field are evaluated at each pixel of the camera. Since the polarization state spatial distribution does not depend on the intensity of the illumination, the polarization-resolved images of the droplets are represented by the reduced Stokes parameters $s_i = S_i/S_0$ ($i = 1, 2, 3$), which all range between -1 and 1 . This is illustrated in Fig. 2 where the s_i images of an $8.5 \mu\text{m}$ diameter radial nematic droplet are shown as a function of the trapping power P_0 .

At low trapping power (see upper row in Fig. 2), we observe a polarization state spatial distribution similar to the one previously reported in [15], which was dedicated to the observation of *phase singularities* generated by radial nematic droplets (see Fig. 3 of [15]). However, there is a fundamental difference, since, here, the polarization-resolved images of the droplets strongly depend on the trapping beam power (see Fig. 2). This is explained by the fact that the trapping light is linearly polarized in the present study, whereas circular

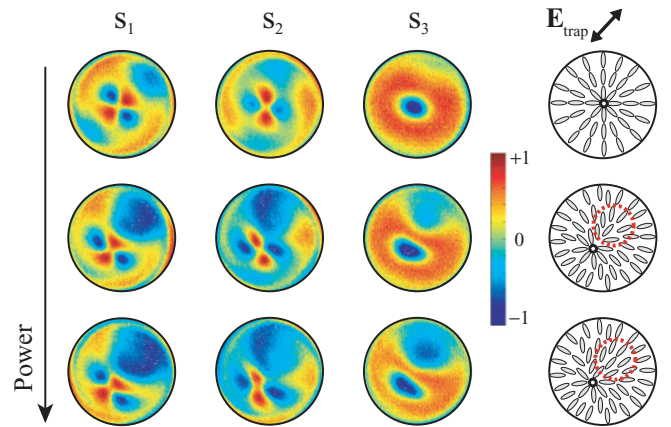


FIG. 2. (Color online) Left part: polarization-resolved images of radial nematic droplets as a function of the trapping power P_0 , where s_1 , s_2 , and s_3 are the reduced Stokes parameters. The droplet diameter is $8.5 \mu\text{m}$ and the upper, middle, and bottom sets of data correspond to $P_0 = 35, 270$, and 540 mW, respectively. Right part: typical director distribution in the equatorial plane of the droplet. At low power the radial alignment is almost unperturbed, whereas it is all the more distorted when the power is increased. The circle marker indicates the location of the hedgehog defect for the director and the dashed circle refers to the region where the director tends to be aligned along the trapping beam polarization plane as a result of laser-induced liquid crystal reorientation.

polarization was used in [15]. Indeed, as detailed in [16], radial droplets are slightly off-center in linearly polarized tweezers in the low power limit in contrast to the circular polarization case, which in turn results in light-induced bulk realignment when the power is increased. This is illustrated in the right part of Fig. 2 where the director distribution changes are sketched. Although the complete description of the laser-induced three-dimensional liquid crystal reordering under tight focusing is a complicated task that is out of the scope of the present study, the qualitative representation given in Fig. 2 can nevertheless be strengthened by looking at the radial droplet as an effective inhomogeneous birefringent parallel slab. Indeed, the introduction of an effective slab model has already been shown to be useful in the context of nematic liquid crystal bipolar droplets [17]. However, in Ref. [17], the effective director distribution can be assumed to be uniform in a satisfying manner, which cannot be done in our case where a hedgehog defect for the director field is present. Therefore, any attempt to describe the optical behavior of a droplet with an effective slab should encompass the space-variant feature of the director.

For this purpose, let us consider a circular uniaxial slab with radius R (that is, the radius of the modeled distorted radial droplet) with a radial distribution of its optical axis in the off-center coordinate system $(xO'y)$. We define the reduced radial coordinates $\rho = r/R$ and $\rho' = r'/R$ in the cylindrical coordinate systems centered on the axes (Oz) and $(O'z)$, which are associated with the polar angles φ and φ' , respectively (see Fig. 3). The reduced offset distance OO' is labeled ρ_0 and, without loss of generality, we may assume that the hedgehog defect for the optical axis distribution is relocated along the x axis as depicted in Fig. 3.

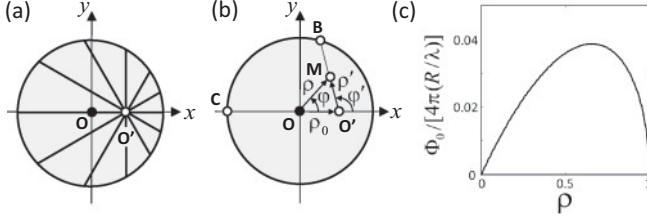


FIG. 3. Definition of the effective inhomogeneous birefringent parallel slab that aims at describing the optical behavior of a possibly distorted radial droplet. (a) Off-axis radial distribution of the optical axis of the slab in the case of a distorted droplet. (b) Definition of the reduced polar coordinates (ρ, φ) and (ρ', φ') associated with the location M in the coordinate systems (xOy) and $(xO'y)$, respectively. The location B refers to the border viewed from the angle φ' in $(xO'y)$ and C corresponds to $B(\varphi' = \pi)$. (c) Φ_0 is a function of ρ in the case of an unperturbed radial droplet for the parameters that correspond to Fig. 4 (see text for values).

Following Ref. [16], the phase delay between the extraordinary and ordinary waves experienced by a ray that propagates along z in an *unperturbed radial droplet* ($\rho_0 = 0$), at distance ρ from its center, is

$$\Phi_0(\rho) = 4\pi \frac{R}{\lambda} \int_0^{\cos \beta(\rho)} \left[\sqrt{\frac{\epsilon_{\parallel} \epsilon_{\perp}}{\epsilon_{\perp} + \epsilon_a \cos^2 \gamma(\rho, \xi)}} - \sqrt{\epsilon_{\perp}} \right] d\xi, \quad (1)$$

where $\beta(\rho) = \arcsin(\rho)$, $\gamma(\rho, \xi) = \arctan(\rho/\xi)$, and $\xi = z/R$ are the reduced coordinates along z . Here, ϵ_{\parallel} and ϵ_{\perp} are the dielectric relative permittivity along and perpendicular to the director and $\epsilon_a = \epsilon_{\parallel} - \epsilon_{\perp}$. The behavior of an unperturbed droplet is therefore described by a birefringent radial slab that induces the phase delay $\Phi_0(\rho)$ at the location M (see Fig. 3). Assuming a right-handed circularly polarized plane wave normally incident onto the inhomogeneous birefringent slab, the expressions for reduced Stokes parameters are conveniently derived using the Jones formalism and one gets

$$s_1 = \sin[\Phi_0(\rho)] \sin 2\varphi, \quad (2)$$

$$s_2 = -\sin[\Phi_0(\rho)] \cos 2\varphi, \quad (3)$$

$$s_3 = -\cos[\Phi_0(\rho)]. \quad (4)$$

The results are shown in Fig. 4(a) for the droplet that corresponds to Fig. 2, where the birefringence of the liquid crystal has been set to 0.07 (and we used the typical value $\sqrt{\epsilon_{\perp}} = 1.5$ for the ordinary refractive index). Such a value is typically 2–3 times lower than the actual birefringence of the nematic liquid crystal 5CB. Such inconsistency has already been reported when effective slab models were proposed in order to describe the behavior of a droplet. Indeed, in experiments, the incident probe light is obviously not a plane wave, and this has drastic consequences on the effective optical anisotropy as noticed in previous works [17,18]. Nevertheless, the main features of the observed patterns are qualitatively obtained.

In the case of a *distorted radial droplet* ($\rho_0 \neq 0$), and in the absence of the knowledge of the director distortion profile, we shall assume that the reduced radial profile of the phase delay in the coordinate system (ρ', φ') is the same as in the

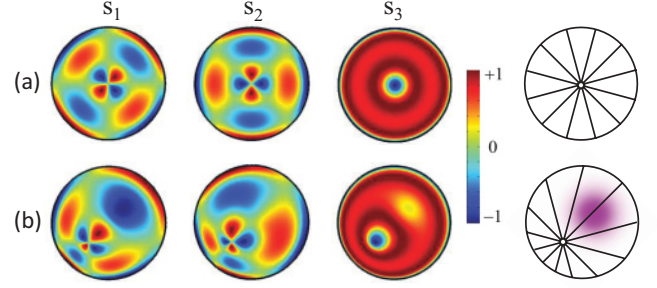


FIG. 4. (Color online) Left part: polarization-resolved images obtained from the inhomogeneous birefringent slab model for the droplet that corresponds to Fig. 2. Right part: spatial distribution of the optical axis of the effective slab is shown on the right part of the figure. (a) Unperturbed radial droplet. (b) Distorted droplet where the shaded area on the right panel refers to the local light-induced birefringence changes $\delta\Phi$ (see text for details).

unperturbed case along each segment $O'B$ (see Fig. 3). To do so, we introduce the radial coordinate $\tilde{\rho} = O'M/O'B$ whose values range from 0 to 1 and which depends on the angle φ' . By definition, we thus have $\tilde{\rho} = \rho'/\rho'_B$ with $\rho' = (\rho^2 - 2\rho\rho_0 \cos \varphi + \rho_0^2)^{1/2}$ and ρ'_B the value of ρ' at location B . Since $\rho_B = 1$, $\rho' \cos \varphi' = \rho \cos \varphi - \rho_0$, and $\rho' \sin \varphi' = \rho \sin \varphi$, we get $\rho'_B = (1 - \rho_0^2 \sin^2 \varphi')^{1/2} - \rho_0 \cos \varphi'$. Therefore, the phase delay can be calculated from the expression

$$\Phi(\rho', \varphi') = \Phi_0(\rho'/\rho'_B). \quad (5)$$

Although Eq. (5) should qualitatively describe the optical transmission properties of the distorted droplet, the realignment ingredient is still missing. The resulting additional phase delay is taken into account by considering a Gaussian-shaped ansatz for the local increase of the birefringence that we arbitrarily assume (i) to be centered in the middle of the segment CO' [Fig. 3(b)] and (ii) to be characterized by a waist ρ_0 . Namely, $\delta\Phi(\rho', \varphi') = \delta\Phi_{\max} \exp[-2\{[\rho' \cos \varphi' + (1 + \rho_0)/2]^2 + (\rho' \sin \varphi')^2\}/\rho_0^2}]$. We finally obtain the Stokes parameters expressions

$$s_1 = \sin[\Phi_0(\rho'/\rho'_B) + \delta\Phi(\rho', \varphi')] \sin 2\varphi', \quad (6)$$

$$s_2 = -\sin[\Phi_0(\rho'/\rho'_B) + \delta\Phi(\rho', \varphi')] \cos 2\varphi', \quad (7)$$

$$s_3 = -\cos[\Phi_0(\rho'/\rho'_B) + \delta\Phi(\rho', \varphi')]. \quad (8)$$

The results are shown in Fig. 4(b), where $\rho_0 = 1/2$ and $\delta\Phi_{\max} = \pi/4$. Note that an appropriate rotation has been applied to the frame definition of Fig. 3 in order to match the actual geometry of Fig. 2. Although empirical, these results emphasize the relevance of the expected director spatial distribution shown in Fig. 2.

In the next section, we show that such light-controlled orientational changes also allow for the observation of the parametric evolution of *polarization singularities* when P_0 is taken as the control parameter.

III. IDENTIFICATION AND TRACKING OF POLARIZATION SINGULARITIES

Recalling that the polarization state of a monochromatic wave is fully determined from the knowledge of the Stokes

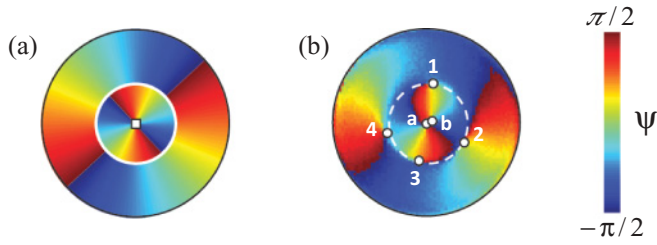


FIG. 5. (Color online) Map of the azimuth angle ψ for an ideal (a) and real (b) radial nematic droplet with $7 \mu\text{m}$ diameter. In the ideal case (a), a nongeneric C point with an index $m = 1$ is located at the origin (square symbol), which is surrounded by a degenerate ring C line (white circle). Instead, in the experiment (b), we observe a set of generic C points (circle symbols): a pair of C points with an index $m = 1/2$ near the origin (labeled as $\{a, b\}$) and two pairs of C points with opposite indices $m = \pm 1/2$ (labeled as $\{1, 2, 3, 4\}$) that qualitatively lie along the ghost of the phase dislocation that would have appeared in the ideal case (dashed circle).

parameters, it is possible to extract from the s_i maps the information on the polarization singularities that are encoded by a LC droplet into the illumination light field emerging from the droplet. For this purpose, we introduce the azimuth angle ψ of the polarization ellipse \mathcal{E} as the angle between the x axis and the major axis of \mathcal{E} (see Fig. 1). The azimuth is evaluated from the expression $\psi = \frac{1}{2} \arctan(s_2/s_1)$ and the C points appear as circularly polarized isolated points around which ψ is continuously rotating. Different kinds of C points exist, which can be classified by using various numbers [19,20]. In particular, the topological index $m = \frac{1}{2\pi} \oint d\psi$ defines the signed total number of counterclockwise rotations of the polarization azimuth around a C point. From a general point of view, generic C points have indices $m = \pm 1/2$; however, one can also have nongeneric C points with $m = 1$, for instance, when a Gaussian beam is propagating along the optical axis of a *spatially homogeneous* uniaxial crystal [21]. In our case, although radial nematic droplets correspond to *spatially inhomogeneous* uniaxial media, the axial symmetry preserves the expected appearance of a nongeneric C point at the origin, as illustrated in Fig. 5(a) by the square symbol.

In the experiment, however, the above-mentioned axial symmetry breaking arising from linearly polarized tweezers even at the lowest trapping power (see Fig. 2) unavoidably lifts the degeneracy of the central nongeneric C point, thereby leading to the appearance of a pair of generic C points with $m = 1/2$. In fact, even if the trapping beam polarization is carefully set as circular, which should preserve the axial symmetry even in presence of optical reorientation (in that case, twisted-radial ordering is expected [16]), we never observe the structurally unstable nongeneric C point. Indeed, any deviation of either the illumination polarization state from the ideal circular case, or the droplet molecular ordering from the radial or twisted-radial ideal configurations, induces a split into two generic C points. This is illustrated in Fig. 5(b) in a situation where we optimized the experimental conditions to preserve the axial symmetry of the “light + matter” system, namely, by using circularly polarized tweezers and selecting well-aligned droplets. As shown in this figure, a pair of generic C points is observed near the origin (see circle symbols labeled $\{a, b\}$) and two

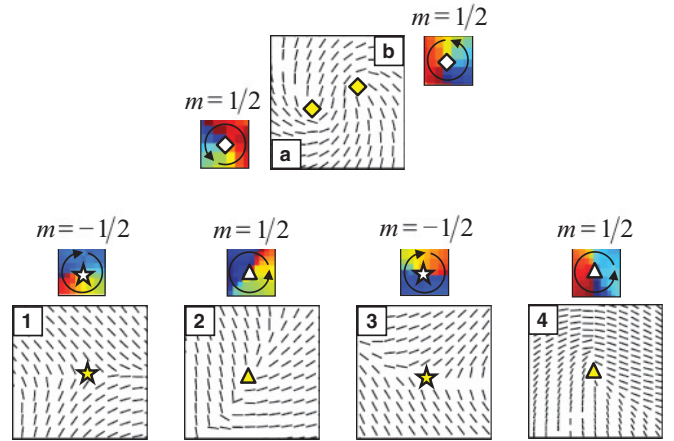


FIG. 6. (Color online) Mapping of the orientation of the polarization ellipse \mathcal{E} in the neighborhood of each of the C points shown in Fig. 5 that are labeled $\{a, b, 1, 2, 3, 4\}$, respectively. The orientation of the major axis of \mathcal{E} is evidenced by a unit vector and the insets refer to the local mapping for the ψ value where the color map is the same as in Fig. 5. Diamonds, stars, and triangles refer to C points of the “lemon” ($m = 1/2$), “star” ($m = -1/2$), and “monstar” ($m = 1/2$) type, respectively. Each box corresponds to a zoom on a $900 \text{ nm} \times 900 \text{ nm}$ area.

pairs of C points with opposite indices $m = \pm 1/2$ (see circle symbols labeled $\{1, 2, 3, 4\}$) are observed instead of the phase dislocation that would have appeared in the ideal case (dashed circle).

Such a set of C points turns out to be the topological fingerprint of the 3D orientational state of the LC droplet. Hence, the idea consists of tracking its evolution as a function of tiny changes of the molecular ordering owing to optically controlled elastic distortions induced by the linearly polarized trapping beam of adjustable power. For this purpose, the first step consists in the unambiguous identification of such a fingerprint. This is done by inspecting the local mapping of the azimuth angle ψ in the neighborhood of each C point as illustrated in Fig. 6, which correspond to Fig. 5, where six C points are clearly identified following the classification given in [20]. Indeed, from [20], we recognize a pair of C points of the “lemon” type near the origin and two pairs of the “star” and “monstar” type C points lie in its surrounding area.

We note that the observations above are closely related to those recently reported in [22,23], where the topology of the space-variant polarization state is studied for nematic films with uniform perpendicular alignment. Nevertheless, in [22,23], the LC axial alignment remains uniform and the spatial evolution of polarization singularities is solely driven by the polarization state of the illumination light. In contrast, in our case, the LC axial alignment is initially nonuniform and is continuously altered via optical orientational nonlinearities driven by the trapping beam power, while the illumination polarization state is fixed as circular.

The evolution of the C points as a function of P_0 is illustrated in Fig. 7(a), which corresponds to the data in Fig. 2, and where only the trajectories of the lemons that initially lie near the center of the droplet at low power are represented [see Fig. 7(b)]. Since the determination of the C points location can

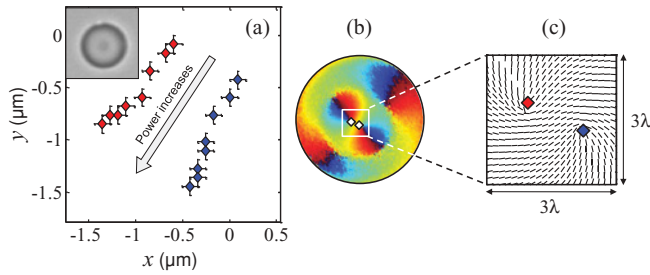


FIG. 7. (Color online) (a) Trajectories of the pair of lemon C points as a function of the linearly polarized trapping beam power. Error bars correspond to ± 1 pixel precision. The set of data corresponds to $P_0 = 35, 90, 150, 210, 270, 330, 390,$ and 540 mW, respectively. Inset: image of the $8.5 \mu\text{m}$ diameter droplet. (b) Azimuth angle mapping of the trapped droplet at $P_0 = 35$ mW. The two diamond symbols refer to the pair of lemons and the color map is the same as in Fig. 5. (c) Local mapping of the major axis of the polarization ellipse on a $3\lambda \times 3\lambda$ area, where $\lambda = 532$ nm is the imaging wavelength. The diamond symbols correspond to those shown in (a).

be obtained with high resolution from the singularities of the ψ map, we easily obtain a 2D subwavelength resolution of their displacements in the observation plane. This is the signature of 3D ordering changes inside the droplet, and it paves the way toward a new strategy for microsensors based on intangible pointlike markers defined as polarization singularities. Indeed, the spatial resolution of polarization singularities imaging is defined by the pixel size rather than the diffraction limit $\sim \lambda$ at the focusing used. The trajectories of singularity points can therefore be resolved at a spatial scale considerably better than λ , as illustrated in Fig. 7(c), showing the local mapping of the major axis of the polarization ellipse on a $3\lambda \times 3\lambda$ area where $\lambda = 532$ nm is the imaging wavelength.

Note that the simple space-variant birefringent slab model presented in Sec. II cannot be used to describe the observations related to polarization singularities. Indeed, to do so, one would need to take into account the nonradial optical axis distribution of a distorted radial droplet in the off-center coordinate system; see the illustration on the right part of Fig. 2.

IV. DISCUSSION

A few remarks can be made in view of expected applications in terms of LC-based microsensors. First, we note that the detection of local changes (here, the position of C points) instead of global ones (e.g., overall intensity changes [5,7,8,24]) has already been implemented in order to improve the sensitivity of a LC sensor. For instance, one can mention the case of nematic layers whose orientational changes are retrieved from the shift of a surface plasmon resonance [25]. The main difference is that strategies based on resonance shifts rely on information localized in the *spectral domain* of the light field, whereas, in our case, a polarization singularity corresponds to optical information encoded in the *spatial domain*. Moreover, we stress that their network could be used as a multidimensional optical signature able to distinguish between different types of surface or bulk orientational changes of the LCs that are related to a chemical or physical signal to detect.

Second, from a general point of view, the intangible tracer concept is related to the optical vortex metrology issue, which was introduced in [26]. It is based on the study of pseudophase singularities in the complex signal representation of a speckle intensity pattern generated by Laguerre-Gauss filtering. Indeed such optical information processing has proved to be efficient and reliable in detecting translational and rotational material displacements [27], fluid flows [28], or animal movements [29]. In contrast, in our case, we are dealing with intangible tracers associated with the polarization degree of freedom of a light field. Moreover, such tracers are actually generated from the propagation of light through a LC sample and do not result from data processing. In addition, the polarization-resolved imaging remains simple to implement experimentally since it does not require the use of interferometric measurement. In particular, recalling that cell membranes are closely related to LCs, the present technique could be applied to identify or monitor the mechanical behavior of biological entities.

Third, we note that the superresolution of optical singularities was recently emphasized in [30] where a polarimetric technique for recording the polarization maps of optical fields was proposed. There, the coaxial superposition of orthogonally polarized reference and signal beams allows the signal phase to be reconstructed from the polarization map of the total field, thereby leading to *superresolution of phase singularities*. In contrast, our method is based on the *superresolution of polarization singularities* and does not require the use of a reference beam. Indeed, we propose a single-beam technique that prevents the fine setup adjustments generally associated with two-beam interferometric methods.

Fourth, the use of 3D LC sensors (i.e., droplets) instead of the standard 2D ones (i.e., films) offers drastic downsizing opportunities that have already been exploited in the context of optical vortex generation at the micrometer scale [15]. Indeed, reconfigurable 3D arrays of microsensors can be envisaged by using dynamical optical tweezers [31], which could be useful for instance in the study of diffusive or convective transport processes in liquids or in the detection of gas gradients.

Finally, we note that a quantitative correlation between 3D changes of the spatial distribution of the optical axis inside a 3D soft-matter-based microsensor and the associated topological network of polarization singularities would be useful. This implies the further development of singular polarimetry [12] in the case of inhomogeneous anisotropic media, which remains an open issue.

V. CONCLUSION

Polarization singularity networks associated with the propagation of light inside inhomogeneous anisotropic media have been proposed to elaborate an alternative optical detection technique for liquid-crystal-based sensors that usually rely on the visual inspection of global intensity changes when the liquid crystalline order has been modified as a result of successful detection. Here, we suggest that the topological polarizational fingerprint embedded in the transverse plane of a probe beam that has passed through a liquid crystal sample can be used to monitor the detection of species or physical constraints able to perturb the initial molecular ordering. We have presented an experimental demonstration based on microscopic nematic droplets in the case where the

orientational changes are controlled by the optical torque density exerted by the trapping beam onto the material. We foresee that the small size of the droplets will allow the realization of reconfigurable, possibly three-dimensional, arrays of microsensors.

From a general point of view, polarization-resolved imaging of liquid crystal droplets manipulated by laser tweezers [32,33] or free droplets, for instance, in microfluidic channels, provides an interface to monitor (macroscopic imaging) liquid crystal order changes occurring at a microscopic scale. Such changes reflect the constraints imposed by the environment on the

droplet, hence, realizing the detection of microscopic events of a different nature (thermal, chemical, optical, or mechanical). It is therefore expected that time-resolved tracking of polarization singularities will bring new opportunities for superresolution optical imaging.

ACKNOWLEDGMENT

This work was supported in part by Grant-in-Aid No. 19360322 from the Ministry of Education, Science, Sports, and Culture of Japan.

-
- [1] L. Torsi, A. Dodabalapur, L. Sabbatini, and P. Zambonin, *Sens. Actuators B* **67**, 312 (2000).
 - [2] B. Crone, A. Dodabalapur, A. Gelperin, L. Torsi, H. E. Katz, A. J. Lovinger, and Z. Bao, *Appl. Phys. Lett.* **78**, 2229 (2001).
 - [3] T. Someya, T. Sekitani, S. Iba, Y. Kato, H. Kawaguchi, and T. Sakurai, *Proc. Natl. Acad. Sci. USA* **101**, 9966 (2004).
 - [4] S. Jung, T. Ji, and V. K. Varadan, *Smart Mater. Struct.* **15**, 1872 (2006).
 - [5] T. J. Novak, R. A. Mackay, and E. J. Poziomek, *Anal. Lett.* **5**, 187 (1972).
 - [6] P. G. de Gennes, *The Physics of Liquid Crystals* (Oxford University Press, Oxford, 1974).
 - [7] V. K. Gupta, J. J. Skaife, T. B. Dubrovsky, and N. L. Abbott, *Science* **279**, 2077 (1998).
 - [8] J. M. Brake, M. K. Daschner, Y.-Y. Luk, and N. L. Abbott, *Science* **302**, 2094 (2003).
 - [9] M. Berry, *Nature (London)* **403**, 21 (2000).
 - [10] J. F. Nye and M. V. Berry, *Proc. R. Soc. London, Ser. A* **336**, 165 (1974).
 - [11] J. F. Nye, *Proc. R. Soc. London, Ser. A* **389**, 279 (1983).
 - [12] K. Y. Bliokh, A. Niv, V. Kleiner, and E. Hasman, *Opt. Express* **16**, 695 (2008).
 - [13] N. Murazawa, S. Juodkazis, S. Matsuo, and H. Misawa, *Small* **1**, 656 (2005).
 - [14] N. Murazawa, S. Juodkazis, and H. Misawa, *J. Phys. D: Appl. Phys.* **38**, 2923 (2005).
 - [15] E. Brasselet, N. Murazawa, H. Misawa, and S. Juodkazis, *Phys. Rev. Lett.* **103**, 103903 (2009).
 - [16] E. Brasselet, N. Murazawa, S. Juodkazis, and H. Misawa, *Phys. Rev. E* **77**, 041704 (2008).
 - [17] C. Manzo, D. Paparo, L. Marrucci, and I. Jánossy, *Phys. Rev. E* **73**, 051707 (2006).
 - [18] S. Juodkazis, S. Matsuo, N. Murazawa, I. Hasegawa, and H. Misawa, *Appl. Phys. Lett.* **82**, 4657 (2003).
 - [19] I. Freund, *Opt. Commun.* **201**, 251 (2002).
 - [20] M. R. Dennis, *Opt. Commun.* **213**, 201 (2002).
 - [21] Y. A. Egorov, T. A. Fadeyeva, and A. V. Volyar, *J. Opt. A: Pure Appl. Opt.* **6**, S217 (2004).
 - [22] A. D. Kiselev, R. G. Vovk, R. I. Egorov, and V. G. Chigrinov, *Phys. Rev. A* **78**, 033815 (2008).
 - [23] I. O. Buinyi, V. G. Denisenko, and M. S. Soskin, *Opt. Commun.* **282**, 143 (2009).
 - [24] M. K. McCamley, G. P. Crawford, M. Ravnik, S. Žumer, A. W. Arntstein, and S. M. Opal, *Appl. Phys. Lett.* **91**, 141916 (2007).
 - [25] B. Kieser, D. Pauluth, and G. Gauglitz, *Anal. Chim. Acta* **434**, 231 (2001).
 - [26] W. Wang, N. Ishii, S. G. Hanson, Y. Miyamoto, and M. Takeda, *Opt. Commun.* **248**, 59 (2005).
 - [27] W. Wang, T. Yokozeki, R. Ishijima, M. Takeda, and S. G. Hanson, *Opt. Express* **14**, 10195 (2006).
 - [28] W. Wang, M. R. Dennis, R. Ishijima, T. Yokozeki, A. Matsuda, S. G. Hanson, and M. Takeda, *Opt. Express* **15**, 11008 (2007).
 - [29] W. Wang, Y. Qiao, R. Ishijima, T. Yokozeki, D. Honda, A. Matsuda, S. G. Hanson, and M. Take, *Opt. Express* **16**, 13908 (2008).
 - [30] V. G. Denisenko, A. Minovich, A. S. Desyatnikov, W. Krolikowski, M. S. Soskin, and Y. S. Kivshar, *Opt. Lett.* **33**, 89 (2008).
 - [31] J. E. Curtis, B. A. Koss, and D. G. Grier, *Opt. Commun.* **207**, 169 (2002).
 - [32] H. Misawa and S. Juodkazis, *Prog. Polym. Sci.* **24**, 665 (1999).
 - [33] E. Brasselet and S. Juodkazis, *J. Nonlinear Opt. Phys. Mater.* **18**, 167 (2009).